Arcus: The Soft X-ray Grating Explorer

Randall K. Smith[a], Margaret Abraham[b], Grace Baird[c], Marshall Bautz[d], Jay Bookbinder[e], Joel Bregman[f], Laura Brenneman[a], Nancy Brickhouse[a], David Burrows[g], Vadim Burwitz[h], Joseph Bushman[c], Claude Canizares[d], Deepto Chakrabarty[d], Peter Cheimets[a], Elisa Costantini[i], Simon Dawson[e], Casey DeRoo[j], Abraham Falcone[g], Adam Foster[a], Luigi Gallo[k], Catherine E. Grant[d], H. Moritz Günther[d], Ralf K. Heilmann[d], Butler Hine[e], David Huenemoerder[d], Steve Jara[e], Jelle Kaastra[i], Ingo Kreykenbohm[l], Kristin Madsen[m], Michael McDonald[d], Michael McEachen[c], Randall McEntaffer[g], Herman Marshall[d], Eric Miller[d], Jon Miller[f], Elisabeth Morse[c], Richard Mushotzky[o], Kirpal Nandra[h], Michael Nowak[p], Frits Paerels[q], Robert Petre[r], Katja Poppenhaeger[s], Andrew Ptak[r], Paul Reid[a], Karolyn Ronzano[e], Jeremy Sanders[h], Mark Schattenburg[d], Jonathan Schonfeld[a], Norbert Schulz[d], Alan Smale[r], Pasquale Temi[e], Lynne Valencic[t], Stephen Walker[e], Richard Willingale[u], Joern Wilms[l], Scott Wolk[a]

[a] Center for Astrophysics | Harvard & Smithsonian, Cambridge, MA USA, [b] The Aerospace Corporation, Pasadena, CA USA, [c] Northrop Grumman, Dulles, VA & Goleta CA USA, [d] Massachusetts Institute of Technology, Cambridge, MA USA, [e] NASA Ames Research Center, Moffet Field, CA USA, [f] University of Michigan, Ann Arbor, MI USA, [g] The Pennsylvania State University, University Park, PA USA, [h] MPI für extraterrestrische Physik, Garching, GE, [i] SRON / Netherlands Institute for Space Research, Utrecht, NL, [j] University of Iowa, Iowa City, IA USA, [k] Saint Mary's University, Halifax, CA,[l] FAU Erlangen-Nuernberg, Bamberg, GE, [m] California Institute of Technology, Pasadena, CA USA, [o] University of Maryland, College Park, MD USA, [p] Washington University, St. Louis, MO USA, [q] Columbia University, New York, NY USA, [r] NASA Goddard Space Flight Center, Greenbelt, MD USA, [s] Leibniz Institute for Astrophysics, Potsdam, GE, [t] Johns Hopkins University, Baltimore, MD USA, [u] University of Leicester, Leicester, UK

ABSTRACT

Arcus provides high-resolution soft X-ray spectroscopy in the 12-50 Å bandpass with unprecedented sensitivity, including spectral resolution > 2500 and effective area > 250 cm². The three top science goals for *Arcus* are (1) to measure the effects of structure formation imprinted upon the hot baryons that are predicted to lie in extended halos around galaxies, (2) to trace the propagation of outflowing mass, energy, and momentum from the vicinity of the black hole to extragalactic scales as a measure of their feedback, and (3) to explore how stars form and evolve. *Arcus* uses the same 12 m focal length grazing-incidence Silicon Pore X-ray Optics (SPOs) that ESA has developed for the *Athena* mission; the focal length is achieved on orbit via an extendable optical bench. The focused X-rays from these optics are diffracted by high-efficiency Critical-Angle Transmission (CAT) gratings, and the results are imaged with flight-proven CCD detectors and electronics. Combined with the high-heritage NGIS LEOStar-2 spacecraft and launched into 4:1 lunar resonant orbit, *Arcus* provides high sensitivity and high efficiency observing of a wide range of astrophysical sources.

1. SCIENCE OF X-RAY GRATING SPECTROSCOPY

1.1 INTRODUCTION

Finding answers to critical open questions in astrophysics posed in the Astro2010 Decadal report requires high-resolution X-ray spectroscopy. Three prominent unsolved queries are: (1) "How do baryons cycle in and out of galaxies, and what do they do while they are there?"(2) "How do black holes grow, radiate, and influence their surroundings?"(3) "How do rotation and magnetic fields affect stars?"
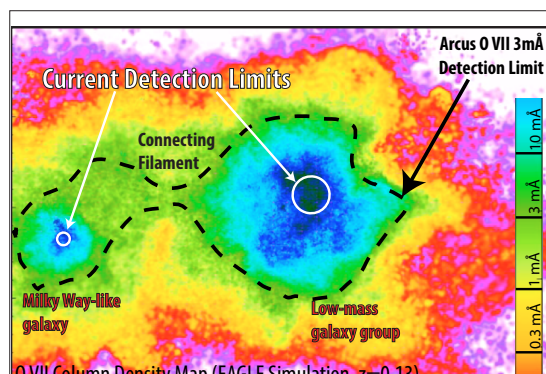
Figure 1 Simulated O VII column density near a low-mass galaxy group and a Milky Way-like galaxy [18].

Figure 2 A demonstration of how baryon census data will measure the slope of the average radial density distribution of Galactic halos to beyond the virial radius. The background QSO (at redshift 0.212) shines through the halos of multiple foreground galaxies (with redshifts from 0.053 to 0.191), imprinting absorption lines from the hot oxygen ions (O VII and O VIII) in each halo along the way (lower inset). These absorption lines appear at their galaxy's redshift, providing a measurement of the amount of gas versus galactocentric radius for each galaxy along the line of sight (top right inset, pink stars). Gathering data from 30-40 AGN fills in the plot. The resulting figure can easily distinguish between models where all of the baryons are found within the virial radius and those where significant baryon fractions exist beyond that point. Currently, reliable data exists only for distances within 50 kpc, equivalent to the first two or three datapoints on the top right inset.
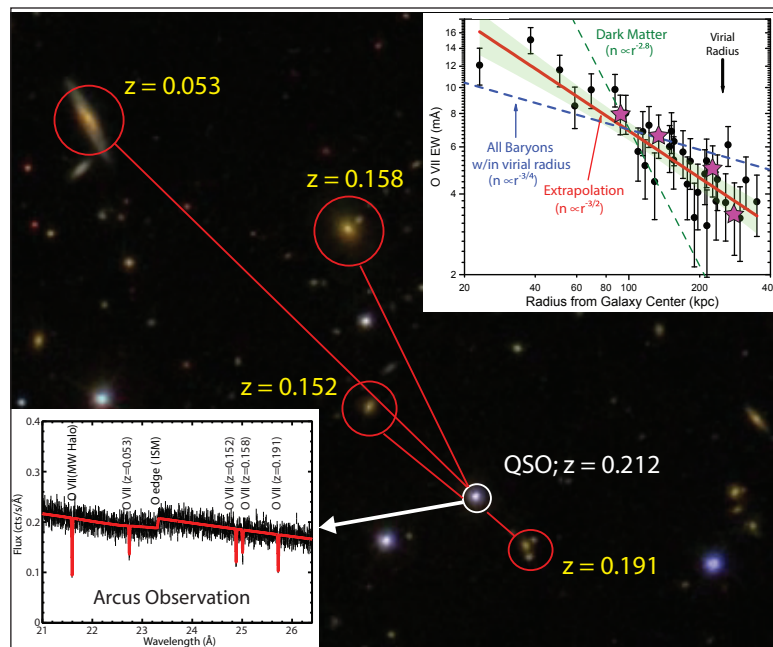
Conducting revolutionary research on these topics requires much higher spectral resolution and effective areas across the 0.25-10 keV X-ray bandpass than available with the current generation of high-resolution X-ray instruments on *Chandra* and *XMM-Newton*. Microcalorimeters such as *XRISM*/Resolve will achieve resolution >1000 with >100 cm² of effective area at energies over 5 keV, only X-ray gratings can achieve this below 2 keV in the near future. The soft X-rays, in particular the bandpass between 0.25-1 keV (12-50 Å), include key diagnostic spectral lines (e.g., O VII, O VIII, Ne IX, S XI) that *Arcus* will use to address a range of scientific goals and priorities set forth by Astro2010 that were reiterated in the NASA Astrophysics Roadmap (2013) and the NASA Strategic Plan (2014). The *Arcus* mission accomplishes these goals at low cost and risk by utilizing newly proven technologies. *Arcus* also complements other high-profile ground and space missions that will be operating in the next decade, including LSST, Euclid, ALMA, JWST and E-ELT/GMT/TMT.

1.2 FINDING AND CHARACTERIZING THE MISSING BARYONS

This objective, set as a high priority in Astro2010, mandates a census of all baryons in the local Universe as a starting point. Numerical simulations indicate that accretion shocks and feedback from supernovae and active galactic nuclei (AGN) naturally result in the production of hot gas in galaxy groups and clusters, as well as galactic halos and the intergalactic filaments that comprise the cosmic web [1,2,3,4; see Figure 1]. These plasmas, collectively referred to as the Warm-Hot Intergalactic Medium (WHIM), are notoriously difficult to observe and are thought to represent the "missing" mass and metal content of the Universe, accounting for half of its baryons and 80-90% of its metals.

At the virial temperature of the hot gas in galaxies, groups and the cosmic web ($10^{5.5}$-$10^{6.8}$ K), nearly all of the dominant ion transitions occur in the X-ray bandpass. As such, X-ray observations of distant, bright point sources absorbed by this intervening gas uniquely measure the WHIM properties. Absorption by O VII, O VIII and other X-ray lines is already detected in the Milky Way halo gas [5,6,7,8] with a column density more than an order of magnitude greater than the lower ionization absorption lines (H I through O VI; [9,10]). However, existing observations lack the sensitivity to determine the fundamental properties of the WHIM in different hosts, as well as the relative roles of critical feedback processes. Within the next decade, *Arcus* is the only observatory capable of measuring the thermal state, dynamics and composition of this hot gas through its absorption signatures imposed on the spectra of background AGN.

The "missing baryon problem" also applies to galaxies. Only 1/4 of the expected baryons are currently accounted for in an L* spiral galaxy [44,45,46], a discrepancy that becomes worse with decreasing galaxy mass. Observations of metals in the local halo are even more extreme and can only account for ~10-15% of the metals expected from star formation [49]. Cool halo clouds detected in the UV account for some of the baryons [47,48], but the rest of the hidden baryons must exist elsewhere. X-ray studies of the Milky Way in absorption and emission, [50] and of external galaxies in emission, [42] indicate that the missing baryons lie beyond the virial radius. Another measure of hot gas, the Sunyaev-Zel'dovich (SZ) effect, also shows that this gas extends beyond the virial radius and can account for all the missing baryons [51]. However,

the SZ data only provides the integrated pressure along a line of sight. When combined with *Arcus* absorption line observations, we will discover the temperature, metallicity and density of this extended gas as a function of radius. Figure 2 [Top Right inset] shows distributions in which (1) the halo gas follows the dark matter distribution ($n \sim r^{-2.8}$), (2) the halo gas follows a density distribution inferred from regions within ~50 kpc of the Milky Way and other galaxies ($n \sim r^{-3/2}$), or (3) the halo gas obeys the flat density law necessary to have all the baryons lie within the virial radius ($n \sim r^{-3/4}$). *Arcus* observations of >30 lines of sight will distinguish between these three cases, including measuring gas column densities to the virial radius and beyond.
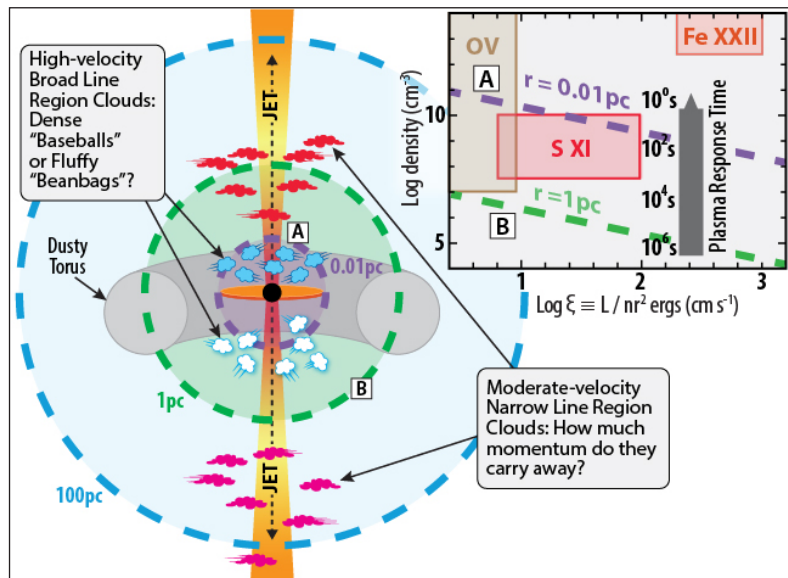
1.3 QUANTIFYING THE IMPACT OF BLACK HOLE WINDS ON THEIR SURROUNDINGS

To determine how galactic-scale outflows from supermassive black holes influence the structure and evolution of the interstellar medium (ISM) and beyond, we must identify the launching mechanism(s) of their winds and mass outflow rates by measuring the wind

Figure 3 A sensitive X-ray grating spectrometer would enable measurements of the properties of the intrinsic absorbing gas present in roughly half of all AGN. The properties of the various absorption lines and their changes in response to changes in the luminosity of the central X-ray source yield the velocity of the outflowing gas and its chemical composition, ionization, density, and distance. Using these parameters we can finally constrain the kinetic power of outflows and quantify their impact on the evolution of the host galaxy.

densities, ionization states and velocities. Comparing outflow properties from the launch point (AGN) to molecular clouds in the host galaxy's ISM is needed to understand fully how such feedback acts on the host galaxy.
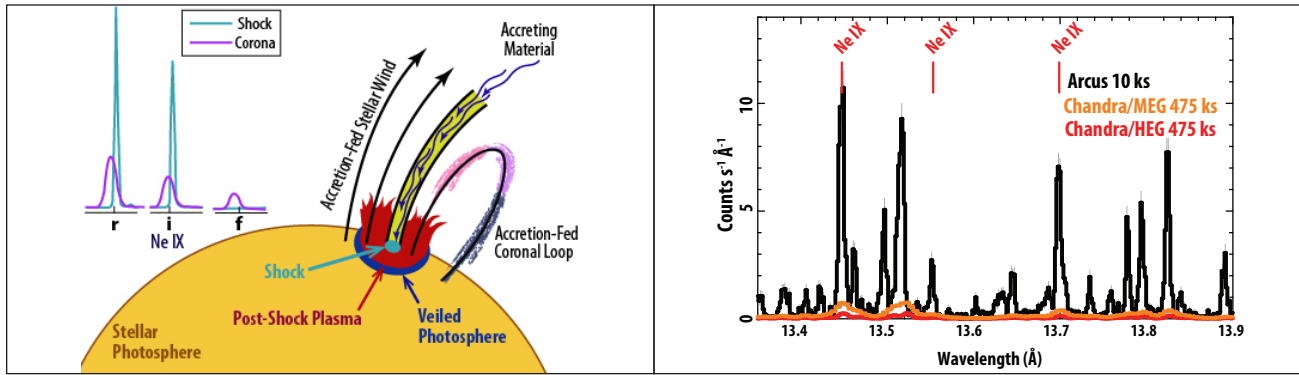
At longer wavelengths, *ALMA* and *JWST* examine the large-scale downstream effects of black hole feedback through observations of dust and cool gas motions. X-ray spectroscopy offers a unique window on these outflows close to their launching points. AGN spectra are most complex at soft X-ray energies, where emission and absorption by dozens of ions in photoionized gas are superimposed on the spectrum. Disentangling these features, which can vary strongly on timescales of days to months, requires an X-ray grating spectrometer with high spectral resolution and with the sensitivity to reveal the velocity distribution, chemical composition, ionization and location of the gas intrinsic to AGN.

Studies of UV and X-ray spectra of AGN show that the column density of the outflow correlates with the ionization of the gas [52]. While UV observations derive precise velocities, they can only measure the small fraction of the gas that has low column densities and low ionization levels. The bulk of the outflow in AGN winds is much more highly ionized and only detectable in X-rays [53,54]. The velocity resolution of the *XMM-Newton* and *Chandra* grating spectrometers (several hundred km s^{-1} in FWHM line width) and their low effective areas allow measurements for only a few of the brightest AGN and require exposure times of >300 ks [55,56,57]. *Athena* will provide much higher area but the resolution of its calorimeter is R < 800 for λ > 6.2 Å, lower than *Chandra* in this bandpass, limiting the features that can be resolved (see Fig. 5).

Arcus's sensitivity to absorption features will enable a qualitative shift in our understanding of AGN outflows. By measuring the ionization of the AGN wind and its response to X-ray continuum flux variations, we can deduce the recombination time of the outflowing gas. This timescale breaks the degeneracy between the gas density and its distance from the AGN, which scales as the ionization parameter $\xi = L/nr^2$, where L is the measured luminosity of the ionizing source, n is the gas density and r is its distance from the ionizing source. Once the density and outflow velocity of the gas are measured, we can then compute the mass outflow rate and kinetic luminosity of the wind (see Figure 3). These two quantities are currently uncertain by orders of magnitude [11], but are constrained to ~30% with *Arcus* observations. These data would also reveal the as-yet-unknown launching mechanism(s) of the wind, e.g., radiative or thermal pressure [12].

Figure 4 An X-ray grating spectrometer can differentiate between the distinct line signatures produced by accretion shocks near the surface vs. those from coronal emission, as seen in the Ne IX emission lines in the schematic on the left. The density, absorbing column, shock velocity, and turbulence of the gas can then be measured using resonance, intercombination, and forbidden lines of He-like ions. At right, we show a comparison of the simulated data from *Arcus* for Capella, as compared with archival data from the *Chandra*/HETG.

## 1.4 EXPLORING THE FORMATION AND EVOLUTION OF STELLAR SYSTEMS

Understanding how magnetic dynamos form coronae over a range of stellar types, ages, and rotation speeds requires measuring the thermodynamic properties of hot gas in stellar magnetic structures and shocks. To gain insight into stellar evolution, we must also probe accretion onto young stars and the atmospheric buildup of exoplanets. The key diagnostics of these processes all occur in the soft X-rays, so a sensitive high-resolution X-ray grating spectrometer is required.

X-ray-emitting coronae are manifestations of magnetic dynamos that operate within the stellar convection zone. *Arcus* explores the evolution of the magnetic dynamo through measurements of both coronal structure and heating for a rich sample of stars of different ages and types. Coronal properties can be determined from X-ray spectra using emission measure distribution (EMD) analysis, which has so far been applied only to the brightest, most active stellar coronae [13], many in binary systems (see Figure 4 [Right]). *Arcus* resolves He-like density diagnostics even in the presence of multiple velocity components, as shown in Figure 4 [Left]. This data will reveal the sizes of coronal structures and any dependencies on stellar age or type [14].

The stellar magnetic field and high-energy radiation from young stars ionize the protoplanetary disk and drive accretion via a magnetorotational instability. They also drive gas motions that catalyze planet formation and migration [15]. During the first ~10 Myr of accretion, the accreting gas absorbs some of the X-ray emission. *Arcus* X-ray spectra can determine the intrinsic flux of this impinging radiation by resolving the emission and absorption components of both the shocked and coronal gas. Further, by determining the X-ray flux from accreting stars onto their protoplanetary disks, such an instrument would quantify how rapidly the high-energy radiation from young stars disperses their gas disks [16], ending the phase of major planet formation.

1.5 X-RAY GRATINGS IN CONTEXT

With the expected launch of *XRISM* in 2022, we are finally poised to achieve R>1000 spectral resolution in the 5-10 keV X-ray bandpass with the Resolve microcalorimeter. If *XRISM* follows a timeline similar to *Suzaku*, we can hope to reap the scientific benefits of this revolutionary detector for ~10 years, providing high-resolution X-ray spectroscopic coverage with ~300 cm² of effective area until the launch of *Athena* in ~2030. The *Athena*/X-IFU microcalorimeter will improve on the *XRISM*/Resolve spatial and spectral resolutions by factors of ~12 and ~2, respectively, and on its effective area by a factor of ~30.
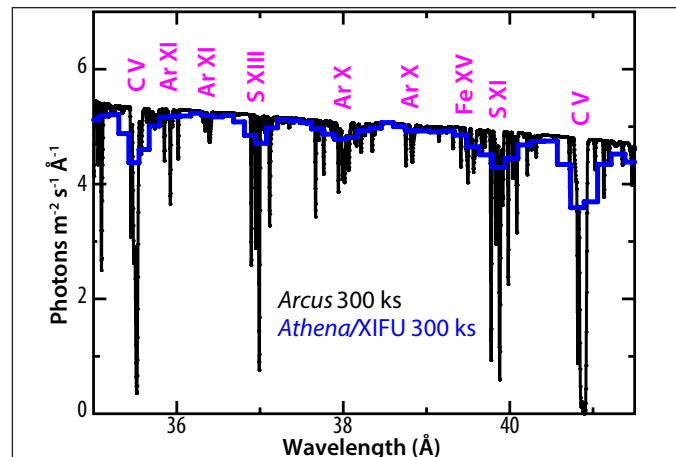
Figure 5 The simulated spectrum of the outflowing wind in NGC 5548, a bright AGN, comparing the resolution of *Arcus* to that of *Athena* in this bandpass.
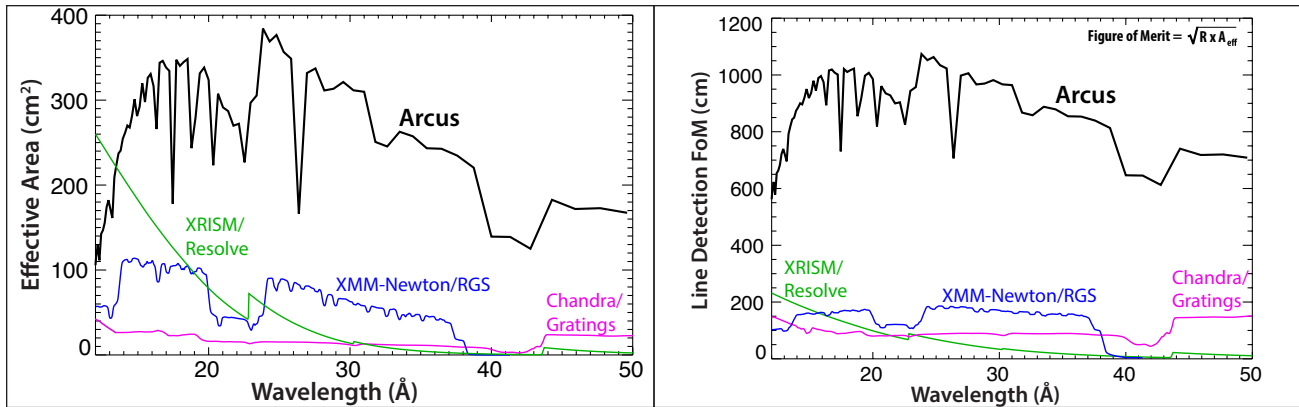
Figure 6 [Left] *Arcus* effective area as a function of wavelength, compared to the *XRISM*/Resolve, *XMM-Newton*/RGS, and the *Chandra* gratings (maximum of LETG/HETG shown). The dips in the *Arcus* area are due to chip gaps. [Right] Figure of merit for detecting weak absorption features, the square root of the product of resolution and effective area. Line detection also scales as sqrt(time), so a 5× decrease in the figure of merit requires 25× more observing time to recover the same sensitivity.

However, neither *XRISM* nor *Athena* includes an X-ray grating spectrometer, thereby losing sensitivity below ~2 keV (see Figure 5) to characterize the missing baryons, to quantify the impact that AGN outflows have on their host galaxies or to fully resolve the mechanisms that drive the formation and evolution of stellar systems. These questions cannot be addressed without a revolution in sensitivity across the X-ray bandpass.

2. TECHNOLOGY

The primary components of an X-ray spectroscopy mission are spectral resolution and area (see Figure 6) combined with efficient observing and low background. *Arcus'* design philosophy addresses the first two using newly demonstrated modular optics and gratings technologies and the latter two with a well-planned mission design. The *Arcus* spectrometer focuses X-rays using SPO Mirror Modules (MMs), which then diffract through the CAT gratings into a spectrum (see Figure 7 Top). The dispersed photons traverse the boom and are detected at the focal plane on one of the two identical Instrument Detector Subassemblies (IDSs). The main components of the spectrometer – the optics, gratings, and detectors – are manufactured using commercial silicon nanofabrication processes, reducing costs and increasing reliability throughout the process.

Arcus leverages substantial, decades-long investments in NASA's development of high-resolution efficient lightweight CAT gratings, and ESA's development of SPO MMs. Combining these technologies provides one to two order-of-magnitude improvements (wavelength-dependent) in spectral resolution and collecting area compared with existing
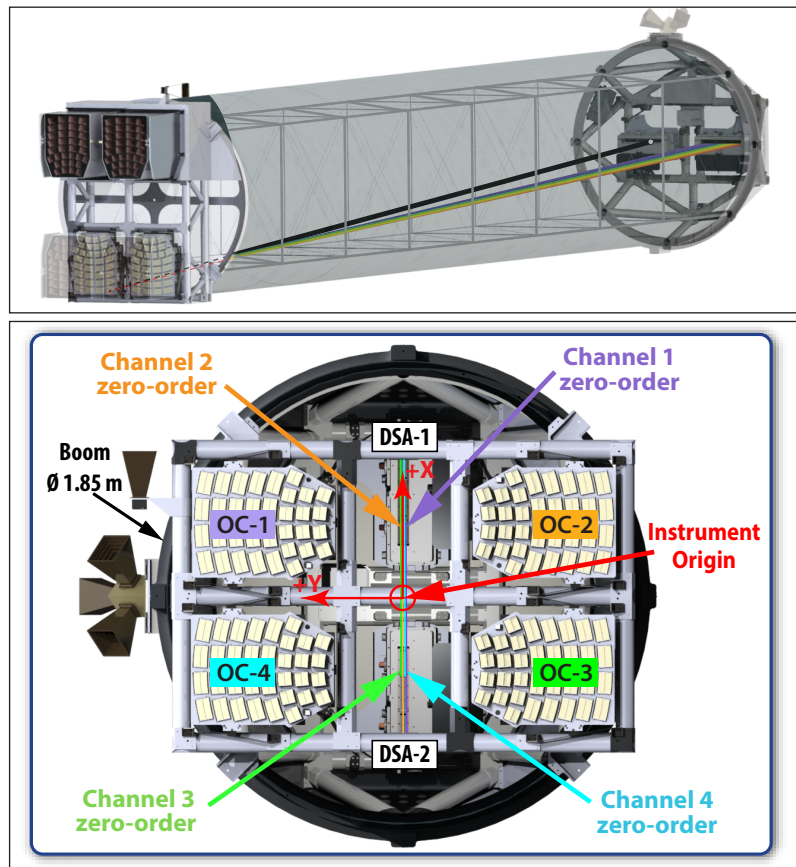
Figure 7 Baseline design incorporating modular optical and grating components.

X-ray spectrometers. *Suzaku*-based CCDs and a *Swift*-based instrument computer provide flight-proven heritage components.

The basic *Arcus* optical design is shown in Figure 7. This is a modular instrument consisting of four optical channels (OCs) and two detector subsystem assemblies (DSAs). The OCs limit the angular span of the telescope aperture to <40°, an approach known as subaperturing [18, 23, 29] allows the design to exploit the anisotropy of the individual SPO MM point spread function (PSF). Aligning the spectrometer's dispersion axis to the narrow axis of the telescope PSF results in a narrow line spread function (LSF) and yields high spectral resolving power.

Figure 8 Sample SPO MM with lightweighted mounting structures.

2.1 Silicon Pore Optics

The SPO MMs (see Figure 8) used for *Arcus* were developed for ESA's *Athena* mission using an automated and modular production system that results in high production efficiency at modest expense [20,21,22]. To simplify production and obtain maximal benefit from ESA's technology development efforts, the SPO MMs on *Arcus* have the same focal length as those on *Athena* and similar radii of curvature. For example, in preparation for the *Athena* mission, flight-like SPO MMs successfully underwent performance testing in an X-ray beamline, and environmental testing for vibration, shock, and thermal response [31, 41]. The only significant difference is in PSF requirements, which take advantage of the naturally asymmetric PSF of the SPOs. As *Arcus* uses the subaperturing technique described above, the PSF in the grating dispersion direction must be <2 arcsec FWHM, while the cross-dispersion PSF need only meet < 21 arcsec FWHM (12 arcsec HEW). The SPO PSF in the dispersion direction easily meets the requirement with a measured value of 1.42 arcsec [17, 34]. For the cross dispersion PSF, at the current best value of 16 arcsec HEW, *Arcus*'s predicted resolution exceeds 2200 and significant improvements are expected as work continues towards the *Athena* PSF requirement of 5 arcsec.

Figure 9 Sample CAT grating aligned and mounted to a Ti base, forming a grating facet.

2.2 Critical-Angle Transmission Gratings

CAT gratings are blazed transmission gratings that combine the high efficiency (30-40%) and resolution (>3000) of blazed reflection gratings with the relaxed alignment tolerances and thermal requirements of conventional transmission gratings [17, 18, 33]. The *Arcus* optical system is designed to take advantage of these relaxed tolerances to simplify integration and reduce costs. The first integration step makes each facet functionally identical and usable anywhere in the *Arcus* aperture. Only this step requires specialized optical measurement tools, in this case a UV Scanning Laser Reflection Tool (SLRT) [37]. The SLRT tracks the orientation of the grating, and allows adjustment for the grating bar angle as the grating is mounted. After the grating facet is assembled, the SLRT is used to verify the grating line spacing uniformity. This ensures that the grating mounting process has not affected the grating. The measurement is also used to predict the grating's contribution to the LSF.
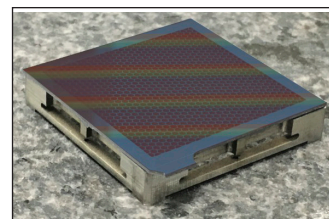
Once mounted, the CAT grating facets have an active area 27 mm × 26 mm (31 mm × 30 mm overall). These individual facets are aligned into CAT Grating Windows (GWs) in either a 2×2 or 2×3 pattern that fully covers the SPO MM they are behind (see Figure 10). This alignment step requires only mechanical, not optical, tolerances (e.g., < 1 mm, <3 arcmin), thanks to the design and alignment done in the previous step. The GWs are then mounted onto the CAT grating petal with similar tolerances. Together, the GWs and petal act to position the facets on a tilted Rowland torus [24, 25, 26, 32] whose toroidal geometry maximizes the spectral resolving power of the *Arcus* spectrometer. The tilt accommodates the grating blaze (defined by the grating bar angle), ensuring that the light is efficiently diffracted to high orders thus providing increased resolving power. The tilt of the Rowland torus reverses for OCs on opposite sides of the instrument Y axis. By matching the torus radii and the grating blaze angle, oblique CAT grating petal pairs (e.g., OC1 & OC3) are rotationally symmetric, which simplifies fabrication. The latest CAT grating technology developments are detailed in [43].

Figure 10 CAT grating windows in two sizes to match SPO widths.
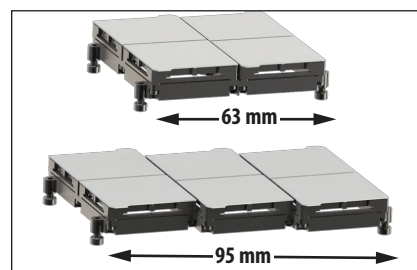
2.3 Optical Alignment

The *Arcus* spectrometer has been modeled in detail using raytracing, a standard approach for simulating X-ray optical systems, with two independently developed raytracing codes [26, 38] that have been verified against laboratory measurements [29]. The raytrace codes have been used to determine the *Arcus*

alignment requirements throughout the system, and, together with the SIXTE [39], were used to predict the final effective area and resolution.

The SPO MMs will be aligned into the SPO petal using the same procedure as developed and tested for *Athena* [27]. Fine alignment is performed under illumination by a planar UV wavefront. By imaging at the 12-m focal plane, an SPO MM can be co-aligned to the previously mounted SPO MMs, ensuring the overall focal length of the completed petal. As each SPO MM is placed in a petal frame, the effect that its PSF has on the combined petal PSF is measured immediately. The SPO MM is then epoxied in place and its alignment is monitored over the cure. Each SPO MM can be removed and replaced if found to be misaligned. This process has already been tested, and found to meet the *Arcus* requirement of increasing the PSF in the dispersion direction by less than 1.5 arcsec HEW [27].

Figure 11 Completed optical channel, combining SPO and grating petal with optical reference cubes.
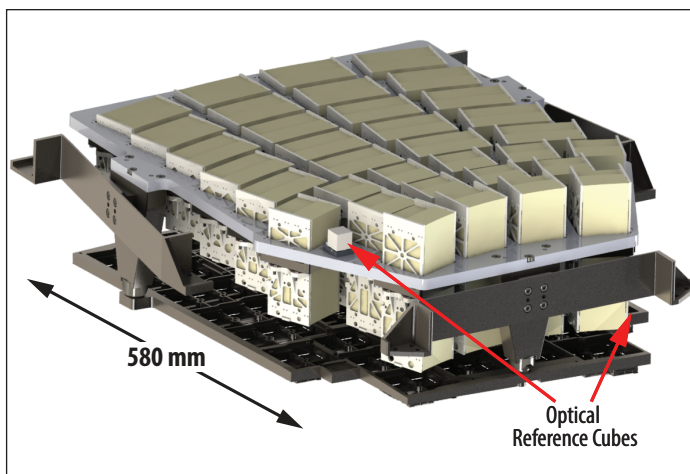
The CAT grating petal is mounted immediately aft of each SPO petal, as shown in Figure 11. The SPO and grating petal assemblies are pre-aligned into OCs using their petal alignment optical references. By design, simple mechanical alignment of the petals will meet OC performance requirements. The *Arcus* team successfully demonstrated this overall approach using two prototype *Arcus* SPO MMs and two GWs (consisting of two grating facets each) at PANTER in 2018 [29].

2.4 Detectors & Focal Plane Electronics

The eight *Arcus* detectors at the heart of each DSA (see Figure 7) collect X-rays from the OCs. These X-rays produce photoelectrons which drift to the CCD buried channel under the influence of internal electric fields. After the 1 s integration time, the collected charge packets are transferred in parallel to a frame store region within 10 ms. The frame store is shielded from focused X-rays. The charge is then transferred to readout nodes, amplified, and read out by the detector electronics before the next CCD readout occurs.

The *Arcus* CCDs are CCID-94 backside illuminated (BI) devices designed and manufactured specifically for *Arcus* by MIT Lincoln Laboratory. They derive directly from the CCID-41 devices flown on *Suzaku* and the CCID-17 devices flown on *Chandra*, and share many design features of those BI detectors: 24 µm pixel size, 45 µm thickness (fully depleted),

Table 1 Arcus Focal Plane Characteristics

Characteristic	Value
Detectors	Back-illuminated frame transfer X-ray CCDs
CCD format	2048x1024, 24 µm pixels [0.41 arcsec/pixel], 8 parallel outputs, chip gaps < 2 mm
Instrument Detector Subsystem (2)	DSA with 8 CCDs and DE
CCD spectral resolution	$\Delta E(FWHM) < 70$ eV at $\lambda = 24$ Å (0.5 keV)
System read noise	<4 e⁻ RMS @ 625 kpixels s⁻¹
CCD frame rate	1 Hz (ensuring negligible pile-up)
Focal plane temperature	-90±0.5 C (passively cooled and controlled)
Optical/UV blocking filter (OBF) Molecular contamination blocking filter (CBF)	Deposited on chip: 40 nm Al On 95% open mesh: 45 nm polyimide plus 30 nm Al

frame store design, and charge injection capability. The 2048×1024 pixel CCDs are identical in height to those previous versions, but twice as wide to more effectively cover the focal plane with fewer devices. Each CCD has 8 output nodes to allow short readout times while clocking sufficiently slowly to ensure low readout noise (<4 e⁻). These characteristics, summarized in Table 1, satisfy the *Arcus* requirements to detect X-ray photons with high efficiency, and determine their energy, arrival time, and detector position. The CCDs are passively cooled and heater controlled to -90±0.5 C like *Chandra*, ensuring adequate spectral resolution for order separation.

The CCD data are transferred to the *Arcus* Instrument Control Unit (ICU), which is responsible for all *Arcus* data processing and formatting, and coordinates all post-commissioning activities on the *Arcus* instrument. The ICU is built by Southwest Research Institute and has heritage from *MMS*/CIDP, *Juno*/JADE, and *Swift*/XRT. A key component of the ICU is the Event Recognition Processor (ERP), whose purpose is to read the CCD image data and extract X-ray events, and in so doing reduce the 418 Mbps data rate into the ERP to a maximum 105 kbps (1.2 kbps average) output [40]. The ERP achieves this reduction by identifying the pixels associated with astrophysical events and reporting data only from them. The ERP uses the same event recognition algorithms employed on the *ASCA*, *Chandra*, *Swift*, and *Suzaku* X-ray observa-

tories. X-rays produce charge clouds in the CCDs that have specific patterns, distinguishing them from charged particles or X-ray pileup (overlapping events during the same exposure). The ERP implements the pattern recognition algorithm in firmware, using a pipelined architecture to attain data processing speeds orders of magnitude higher than those attainable using the software solutions of the heritage missions, allowing the ERP to handle *Arcus'* much higher pixel count.

2.5 Boom

The 12 m *Arcus* focal length requires an extensible boom. We selected an NGIS Goleta coilable boom because the technology provides a light, cost effective, and stable deployable optical bench and it has the most flight heritage of any deployable boom system (51 successful flight deployments). The chosen design is similar to the one developed for the Gravity and Extreme Magnetism Small Explorer (*GEMS*) mission, scaled to *Arcus'* requirements. The 12 m focal length requires a deployable boom approximately 10.82 m long with a clear optical passage down the center of at least 1.85 m in diameter (see Figure 7 [Top]). To meet *Arcus* imaging requirements, the deployable boom must open predictably and maintain its alignment on timescales shorter than 6 ks when subject to the orbital thermal environment. Secondary considerations include minimizing stowed size, weight, and design and deployment complexity. The selected boom uses 4 continuous low CTE (<0.15 ppm/C) pultruded carbon fiber reinforced polymer longerons arranged in a square shape. The boom stows to 2% of its deployed length, and the strain energy stored in buckling provides the deployment force.

Simulations performed during Phase A show that the 1.85-m diameter *Arcus* boom, with its harness and enclosed in a Germanium Black Kapton® light-suppressing sock has a first mode 1.5 Hz (cantilever around Y). In full observatory simulations, including the boom, sock and harnesses, the Attitude Determination and Control System (ADCS) performance met requirements. The boom repeatability performance predictions were based on scaling the *GEMS* boom EM performance and then confirmed on a full-sized *Arcus* boom. Boom motions between the front and rear instrument assemblies will be measured by the zero-order image from the source, potentially complemented by a metrology system such as that on *Hitomi* or *NuSTAR*.

3. MISSION DESIGN

3.1 Overview

Arcus meets the requirement for high efficiency observing from a stable platform via a 4:1 lunar resonant orbit. The mission design enables continuous operations, and the ~6.8-day period High Earth Orbit (HEO) provides a benign radiation environment, low disturbance torques, and long-term orbit stability. Science operations are simple, with long, low-jitter, inertially-pointed observations. The simplicity of operations in the HEO environment leads to a high (>84%) observing efficiency ensuring that all science observations can be accomplished within 18 months of the 2-year baseline science phase, providing 6 months of margin. The flight system consumables are sized for 10 years to enable possible extended operations.

3.2 Spacecraft

A high-heritage NGIS spacecraft (S/C) meets all instrument and mission requirements with robust technical margins. *Arcus* uses the LEOStar-2 S/C bus as its core and the basis for its ADCS, command and data handling (C&DH), telecom, power, and thermal subsystems, allowing substantial reuse of *TESS* and *ICON* GSE. The *Arcus* S/C at launch is <4 m high with a diameter <2 m and a total mass of <1200 kg, comfortably fitting within the capabilities of the standard launch vehicle services provided for MIDEX missions (see Figure 12). The S/C provides continuous power to the instrument, with batteries designed to survive worst-case eclipses. The S/C connection to the Rear Assembly of the instrument is thermally isolated. This bus is also used by *NuSTAR* with a similar instrument configuration and has been adapted for the *TESS* mission to the HEO environment.

The *Arcus* ADCS design is driven by the requirement to provide a highly stable platform (relative attitude stability at the detectors mounting < 2 arcsec/axis over 1 second, 3σ) for the *Arcus* instrument configuration, with sufficient absolute pointing control (40 arcsec/axis, 3σ) for science target observation. The design incorporates selective redundancy to support a possible extended mission. The selected orbit's dominant disturbance torque is solar radiation pressure acting on the Cp-Cg offset of >1.8 m, as gravity gradient is minimal in HEO. The only agility requirement is to limit the duration of slews between targets to improve observing efficiency (< 180 min for
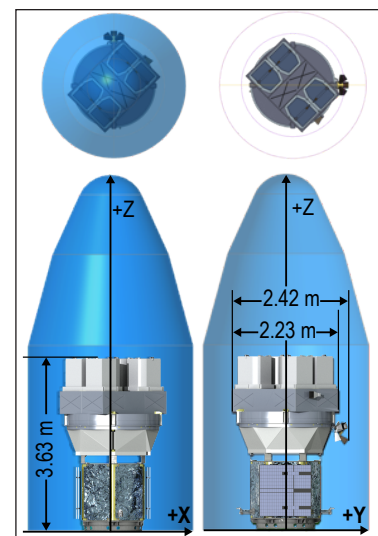
Figure 12 Arcus in typical MIDEX LV fairing has good margins.
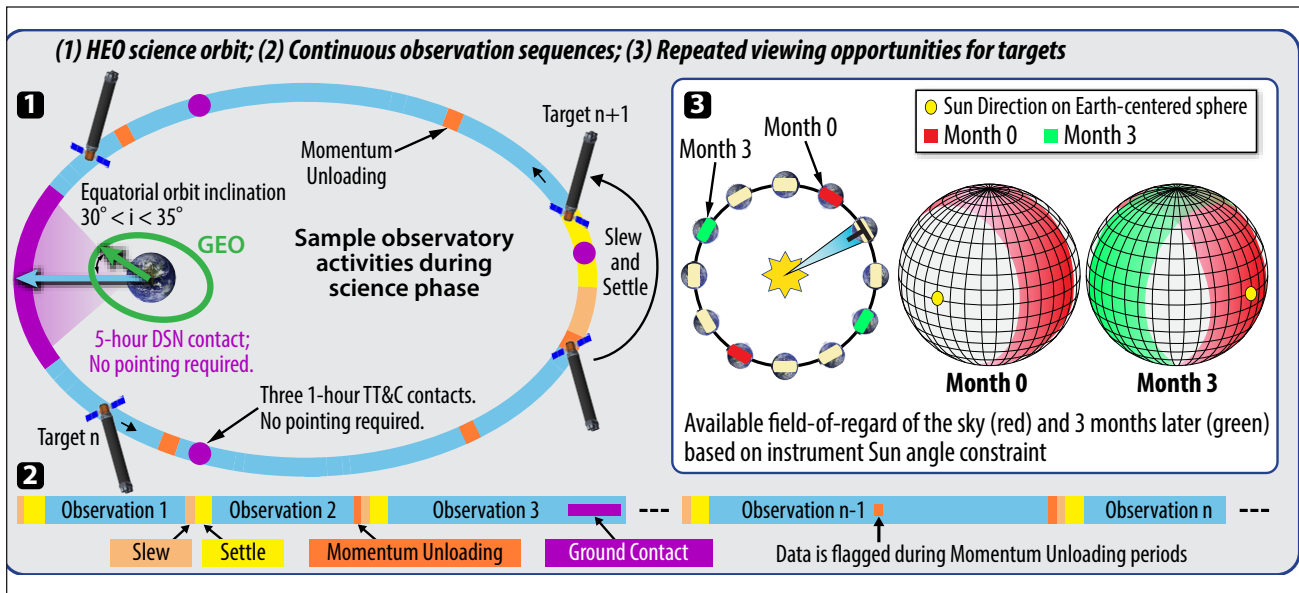
Figure 13 The *Arcus* orbit enables a straightforward observing cadence with multiple opportunities to observe targets, which are not time-sensitive.

180° in any axis). It is met with excellent margins by the selected heritage reaction wheel assemblies providing fine pointing control with low jitter and adequate momentum storage with margin. The 3-axis stabilized system maintains attitude stability and control throughout all mission phases using well-understood hardware and flight software with flight-proven ADCS algorithms.

4.0 OPERATIONS

4.1 Overview

The *Arcus* science requirements can be achieved with observations of a well-defined target list with ~300 sources that are not time-constrained and can be observed in any order. The approximately 76,000 x 215,000 km altitude science orbit is shown in Figure 13. It is a 4:1 lunar resonant HEO, similar to the *TESS* 2:1 orbit but with an ~6.8 day period. This orbit maximizes observation time and enables the completion of all science objectives within the 2-year baseline science phase by providing:

- Large field-of-regard with multiple targets available at any one time;
- Low radiation environment, avoiding the Van Allen belts at all times;
- Low disturbance torques from either the Earth or Moon;
- No orbit maintenance maneuvers;
- Relatively few eclipses;
- Maximum eclipse duration of 4.5 hours;
- Near-continuous line of sight to ground stations; and
- Thermally stable conditions.

Instrumental pointing is limited to 90°±25° from the Sun, which is required for thermal and power reasons, as pointing at angles outside of this limit decreases the thermal balance and increases the power demands of the heaters. This is the primary constraint on the field of regard (see Figure 13 [Right]).

4.2 Mission Operations

As most *Arcus* observations are a day or longer, the selected orbit allows a stable and simple cadence for mission operations. After commissioning, real-time contacts with the S/C via the Deep Space Network (DSN) are performed once per orbit near perigee for science data download (SDDL) and for uploading a 2-week long observation schedule. No re-pointing

is required for this or the three Tracking, Telemetry & Commanding (TT&C) contacts that occur at other points in the orbit. Science data processing reuses software and algorithms developed for *Chandra*, *Suzaku*, and *eRosita*.

NASA/ARC hosts the *Arcus* Mission Operations Center (MOC) as part of the ARC Multiple Mission Operations Center (MMOC). The ARC MMOC has successfully managed mission operations for a number of Explorer-class missions such as *Kepler*, *LCROSS*, *LADEE*, and *IRIS*, providing both experi-

Figure 14 Experienced operations teams have a well-understood plan to achieve mission success.

ence and flexibility at modest expense. The MOC is led by the Mission Operations Manager and contains multiple teams, including the Flight Director team that leads operations and the Real Time Operations (RTO) team. Flight Dynamics and Mission Planning and Sequencing work in conjunction with RTO, providing the necessary planning and analysis products. The Spacecraft Support Team (SST) is made up of subsystem experts that supported earlier project phases. Initially the SST will support MOS from the MOC and provide critical efforts during the S/C activation and checkout. Once the instrument has been completely activated, the SST will move to an on-call roll from the Spacecraft Support Center. Finally, Ground Data System support is provided as a service by the MMOC. With the S/C bus and instrument in good working order, the near weekly cycle for the MOS elements, centered on SSDL, begins. This cadence allows MOC teams to reduce to a smaller, single-shift which is sufficient for the repeated cadence of activities in the science phase.

The instrument captures science data continuously, except during an eclipse. Data acquired during attitude slews, momentum unloadings, and before and after eclipse when outside of operational temperatures, are flagged for post-processing. Ground contacts do not interrupt or affect science observations. Planning and data processing follow the same routine each week, centered on the science data downlink contact (see Figure 14). During this contact, the MOC downlinks all stored data, uploads a new command sequence, and performs health and status checks on real-time telemetry. The day after each SDDL, the MOC analyzes downlinked housekeeping data with the Data Trending System. The Science Operations Center (SOC) completes the science data processing with the science pipeline software and makes an initial assessment of data quality to determine if updates to the observation plan are required. V&V and science team quality/calibration checks continue in parallel with subsequent orbit cycles.

4.3 Science Operations

The Smithsonian Astrophysical Observatory (SAO) provides the SOC, working closely with ARC. SAO hosts and operates multiple science operations centers ranging in scale from Explorer-sized (*Hinode*) to flagship (*Chandra*). The Science Operations Team (SOT), located at the Science Operations Center (SOC), is led by the Science Operations Manager (SOM) and includes experts in science operations and the instrument. As a whole, the SOT ensures the science goals are met during the flight mission. The SOT is responsible for generating observation plans and processing science data. The Instrument Support Team (IST) contains subject matter experts on the instrument hardware, design, and performance. The IST will provide low support levels during early flight phases, ramping up to full staffing during instrument activation and commissioning. Once instrument commissioning is completed, support levels will drop to match calibration activities with wider on-call support available for anomaly resolution.
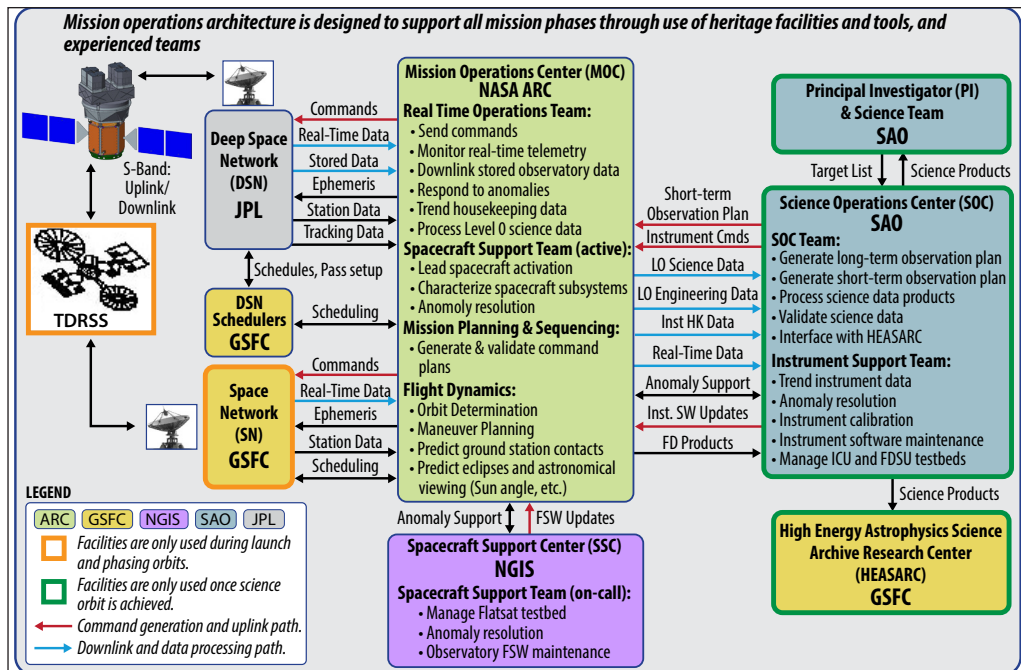
The SOC staff runs the pipeline software, generating a range of data products from Level 0 through Level 2. Level 0 data contain CCD position, frame, grade, and pulse height as produced by the ICU ERP, as well as raw star tracker and metrology measurements, and other S/C ancillary data, providing context to the observations. These are generated at the MOC and sent to the SOC. The pipeline software uses these Level 0 data as input to generate the downstream data products. All data are kept in standard FITS format. Level 1 event data take the Level 0 data and format the header keywords and table columns to match the format used throughout the pipeline processing. Level 1a data then incorporate the detector calibration information to convert event pulse heights into energy values and calculate the aspect solution and good time intervals (GTI). The pipeline software then combines these with further calibration data (e.g., focal length, grating period), enabling calculation of the dispersion coordinate (order × wavelength), and the cross-dispersion coordinate to generate Level 1b data. GTIs are factored in to produce Level 2 event lists. From these event lists ,the pipeline software ultimately generates spectra and ancillary data in standard format files, facilitating analysis with off-the-shelf data manipulation packages such as HEAsoft. The pipeline software has strong heritage from various existing missions. The Level 0 & 1 pipeline is based on the *eROSITA* NRTA package, while higher levels are based on the HEAsoft suite used by X-ray Explorer missions such as *Swift*, *NuSTAR* and *Hitomi*, with algorithms from the *Chandra* grating analysis model.

Acknowledgements

5.0 REFERENCES

[1] Smith, B. D., et al., "The Nature of the Warm/Hot Intergalactic Medium. I. Numerical Methods, Convergence, and O VI Absorption", The Astrophysical Journal, vol. 731, p. 6 (2011).

[2] Cen, R., "Coincidences between O VI and O VII Lines: Insights from High-resolution Simulations of the Warm-hot Intergalactic Medium", The Astrophysical Journal, vol. 753, p. 17 (2012).

[3] Marinacci, F., et al., "Diffuse gas properties and stellar metallicities in cosmological simulations of disc galaxy formation", Monthly Notices of the Royal Astronomical Society, vol. 442, p. 3745 (2014).

[4] Schaye, J., et al., "The EAGLE project: simulating the evolution and assembly of galaxies and their environments", Monthly Notices of the Royal Astronomical Society, vol. 446, p. 521 (2015).

[5] Nicastro, F., et al., "Chandra Discovery of a Tree in the X-Ray Forest toward PKS 2155-304: The Local Filament?", The Astrophysical Journal, vol. 573, p. 157 (2002).

[6] Rasmussen, A., Kahn, S. M., and Paerels, F., "X-ray IGM in the Local Group" in "The IGM/Galaxy Connection. The Distribution of Baryons at z=0", proceedings of the Astrophysics and Space Science Library, vol. 281, p. 109 (2003).

[7] Wang, Q. D., et al., "Warm-Hot Gas in and around the Milky Way: Detection and Implications of O VII Absorption toward LMC X-3", The Astrophysical Journal, vol. 635, p. 386 (2005).

[8] Miller, M. J., and Bregman, J. N., "The Structure of the Milky Way's Hot Gas Halo", The Astrophysical Journal, vol. 770, p. 118 (2013).

[9] Fox, A. J., et al., "Multiphase High-Velocity Clouds toward HE 0226-4110 and PG 0953+414", The Astrophysical Journal, vol. 630, p. 332 (2005).

[10] Wakker, B. P., et al., "Characterizing Transition Temperature Gas in the Galactic Corona", The Astrophysical Journal, vol. 749, p. 157 (2012).

[11] King, A. L., et al., "Regulation of Black Hole Winds and Jets across the Mass Scale", The Astrophysical Journal, vol. 762, p. 103 (2013).

[12] Miller, J. M., et al., "The magnetic nature of disk accretion onto black holes", Nature, vol. 441, p. 953 (2006).

[13] Cohen, D. H., et al., "Measuring the shock-heating rate in the winds of O stars using X-ray line spectra", Monthly Notices of the Royal Astronomical Society, vol. 444, p. 3729 (2014).

[14] Testa, P., Drake, J. J., and Peres, G., "The Density of Coronal Plasma in Active Stellar Coronae", The Astrophysical Journal, vol. 617, p. 508 (2004).

[15] Hartmann, L., Herczeg, G., and Calvet, N., "Accretion onto Pre-Main-Sequence Stars", Annual Review of Astronomy and Astrophysics, vol. 54, p. 135 (2016).

[16] Owen, J. E., Ercolano, B., and Clarke, C. J., "Protoplanetary disc evolution and dispersal: the implications of X-ray photoevaporation", Monthly Notices of the Royal Astronomical Society, vol. 412, p. 13 (2011).

[17] Heilmann, R. K., et al., "Critical-angle transmission grating technology development for high resolving power soft x-ray spectrometers on Arcus and Lynx", proceedings of the SPIE Conference Series, vol. 10399, p. 1039914 (2017).

[18] Heilmann, R. K., et al., "Critical-angle x-ray transmission grating spectrometer with extended bandpass and resolving power > 10,000" in "Space Telescopes and Instrumentation 2016: Ultraviolet to Gamma Ray", proceedings of the SPIE, vol. 9905, p. 99051X (2016).

[19] Bookbinder, J. et al., "The International X-ray Observatory - RFI#1", ArXiv e-print #1001.2329 (2010)

[20] Bavdaz, M., et al., "The ATHENA telescope and optics status", proceedings of the SPIE Conference Series, vol. 10399, p. 103990B (2017).

[21] Collon, M. J., et al., "Development of ATHENA mirror modules", proceedings of the SPIE Conference Series, vol. 10399, p. 103990C (2017).

[22] Valsecchi, G., et al., "Optical integration of SPO mirror modules in the ATHENA telescope", proceedings of the SPIE Conference Series, vol. 10399, p. 103990E (2017).

[23] Cash, W., "X-ray optics - A technique for high resolution imaging", Applied Optics, vol. 26, p. 2915 (1987).

[24] Beuermann, K. P., Braeuninger, H., and Truemper, J., "Aberrations of a facet-type transmis- sion grating for cosmic X-ray and XUV spectroscopy", Applied Optics, vol. 17, p. 2304 (1978).

[25] Paerels, F., "X-ray Diffraction Gratings for Astrophysics", Space Science Reviews, vol. 157, p. 15 (2010).

[26] Günther, H. M., Frost, J., and Theriault-Shay, A., "MARXS: A Modular Software to Ray-trace X-Ray Instrumentation", The Astronomical Journal, vol. 154, p. 243 (2017).

[27] Valsecchi, G. et al., "Results of Silicon Pore Optics Mirror Modules Optical Integration in the Athena Telescope" proceedings of the SPIE Conference Series, vol. 10699-34 (2018)

[28] Bruccoleri, A.R., Heilmann, R.K., Schattenburg, M.L. "Fabrication process for 200 nm-pitch polished freestanding ultrahigh aspect ratio gratings," , J. Vac. Sci. Technol. B 34, 06KD02 (2016).

[29] R.K. Heilmann, A.R. Bruccoleri, J. Song, et al., "Blazed transmission grating technology development for the Arcus x-ray spectrometer explorer,", Proc. SPIE 10699, 106996D (2018).

[30] Kaplan, Alex F., Gilbert, Jason A., Trabert, Rachel, Zurbuchen, Thomas H. and Guo, L. Jay "Free-standing silicon nanogratings for extreme UV rejection," , ACS Photonics 1, 554−559 (2014)

[31] Landgraf, B. et al.,"Environmental testing of the Athena mirror modules" Proc. SPIE 10399 (2017)

[32] H. M. Günther et al.,"Ray-tracing Arcus in Phase A", Space Telescopes and Instrumentation 2018: Ultraviolet to Gamma Ray, J.-W. A. den Herder, S. Nikzad, K. Nakazawa (eds.), Proc. SPIE 10699, 106996F 1-20 (2018).

[33] R. K. Heilmann, J. Kolodziejczak, A. R. Bruccoleri, J. A. Gaskin, and M. L. Schattenburg, "Demonstration of Resolving Power $\lambda/\Delta\lambda > 10,000$ for a Space-Based X-ray Transmission Grating Spectrometer" Appl. Opt. 58, 1223-1238 (2019).

[34] Smith, R. K., et al., " Arcus: The X-ray Grating Spectrometer Explorer ", proceedings of the SPIE Conference Series, vol. 10399, p. 1039914 (2017).

[35] Collon, M. J., et al., "Development of ATHENA mirror modules", proceedings of the SPIE Conference Series, vol. 10399, p. 103990C (2017).

[36] Collon, M. J. et al., " Silicon pore optics mirror module production and testing", Proceedings of the SPIE, Volume 10699, id. 106990Y (2018).

[37] Song, J. et al. "Metrology for quality control and alignment of CAT grating spectrometers", Proceedings of the SPIE, Volume 10699, id. 106990S (2018)'

[38] Swarm, D., DeRoo, C., and Smith, R. K. "Modeling Arcus optical performance using cluster computing", Proceedings of the SPIE, this volume

[39] Wilms, J. et al. "Arcus end-to-end simulations", American Astronomical Society Meeting Abstracts #231, 237.22

[40] Burrows, D. et al. "Fast event recognition for x-ray silicon imagers", proceedings of the SPIE, vol. 9905, p. 99050L (2016).

[41] Wille, E. et al., "Stray Light Baffling and Environmental Qualification of Silicon Pore Optics", Proceedings of the SPIE, vol. 8861, 88611E (2013)

[42] Bregman, J. N., et al., "The Extended Distribution of Baryons Around Galaxies", Astrophysical Journal, vol. 862, p. 3 (2018).

[43] Heilmann, R. K. Schattenburg, M. L., Bruccoleri, A. R., Song, J. "Progress in x-ray critical-angle transmission grating technology", Proceedings of the SPIE, this volume, 11119-39

[44] Moster, B. P., et al., "Constraints on the Relationship between Stellar Mass and Halo Mass at Low and High Redshift", The Astrophysical Journal, vol. 710, p. 903 (2010).

[45] McGaugh, S. S., et al., "The Baryon Content of Cosmic Structures", The Astrophysical Journal Letters, vol. 708, p. L14 (2010).

[46] Dai, X., et al., "XMM-Newton Detects a Hot Gaseous Halo in the Fastest Rotating Spiral Galaxy UGC 12591", The Astrophysical Journal, vol. 755, p. 107 (2012).

[47] Stocke, J. T., et al., "Characterizing the Circumgalactic Medium of Nearby Galaxies with HST/COS and HST/STIS Absorption-line Spectroscopy", The Astrophysical Journal, vol. 763, p. 148 (2013).

[48] Werk, J. K., et al., "The COS-Halos Survey: Physical Conditions and Baryonic Mass in the Low-redshift Circumgalactic Medium", The Astrophysical Journal, vol. 792, p. 8 (2014).

[49] Shull, J. M., Danforth, C. W., and Tilton, E. M., "Tracing the Cosmic Metal Evolution in the Low-redshift Intergalactic Medium", The Astrophysical Journal, vol. 796, p. 49 (2014).

[50] Li, Y., and Bregman, J., "The Properties of the Galactic Hot Gaseous Halo from X-Ray Emission", The Astrophysical Journal, vol. 849, p. 105 (2017).

[51] Singh, P., et al., "X-ray and SZ constraints on the properties of hot CGM", ArXiv e-print 1801.06557 (2018).

[52] Crenshaw, D. M., and Kraemer, S. B., "Feedback from Mass Outflows in Nearby Active Galactic Nuclei. I. Ultraviolet and X-Ray Absorbers", The Astrophysical Journal, vol. 753, p. 75 (2012).

[53] Behar, E., "Density Profiles in Seyfert Outflows", The Astrophysical Journal, vol. 703, p. 1346 (2009).

[54] Arav, N., et al., "Multiwavelength campaign on Mrk 509. X. Lower limit on the distance of the absorber from HST COS and STIS spectroscopy", Astronomy and Astrophysics, vol. 544, p. A33 (2012).

[55] Kaspi, S., et al., "The Ionized Gas and Nuclear Environment in NGC 3783. I. Time-averaged 900 Kilosecond Chandra Grating Spectroscopy", The Astrophysical Journal, vol. 574, p. 643 (2002).

[56] Kaastra, J. S., et al., "Multiwavelength campaign on Mrk 509. VIII. Location of the X-ray absorber", Astronomy and Astrophysics, vol. 539, p. A117 (2012).

[57] Kaastra, J. S., et al., "A fast and long-lived outflow from the supermassive black hole in NGC 5548", Science, vol. 345, p. 64 (2014).